Journal of Organometallic Chemistry 943 (2021) 121816

Contents lists available at ScienceDirect

Journal of Organometallic Chemistry

journal homepage: www.elsevier.com/locate/jorganchem

Proton reduction by phosphinidene-capped triiron clusters ☆

Ahibur Rahaman [a,*], George C. Lisensky [b], Matti Haukka [c], Derek A. Tocher [d], Michael G. Richmond [e], Stephen B. Colbran [f,*], Ebbe Nordlander [a,*]

[a] Chemical Physics, Department of Chemistry, Lund University, Box 120, SE-221 00 Lund, Sweden
[b] Department of Chemistry, Beloit College, 700 College Street, Beloit, WI 53511, USA
[c] Department of Chemistry, University of Jyväskylä, Box 111, FI-40014, Jyväskylä, Finland
[d] Department of Chemistry, University College London, 20 Gordon Street, London WC1H OAJ, UK
[e] Department of Chemistry, University of North Texas, Denton, TX 76203, USA
[f] School of Chemistry, University of New South Wales, Sydney, NSW 2052, Australia

ARTICLE INFO

Article history:
Received 7 February 2021
Revised 29 March 2021
Accepted 5 April 2021
Available online 20 April 2021

Keywords:
Triiron
Phosphinidine
Electrocatalysis
Proton reduction
DFT

ABSTRACT

Bis(phosphinidene)-capped triiron carbonyl clusters, including electron rich derivatives formed by substitution with chelating diphosphines, have been prepared and examined as proton reduction catalysts. Treatment of the known cluster $[Fe_3(CO)_9(\mu_3\text{-}PPh)_2]$ (1) with various diphosphines in refluxing THF (for 5, refluxing toluene) afforded the new clusters $[Fe_3(CO)_7(\mu_3\text{-}PPh)_2(\kappa^2\text{-dppb})]$ (2), $[Fe_3(CO)_7(\mu_3\text{-}PPh)_2(\kappa^2\text{-dppv})]$ (3), $[Fe_3(CO)_7(\mu_3\text{-}PPh)_2(\kappa^2\text{-dppe})]$ (4) and $[Fe_3(CO)_7(\mu_3\text{-}PPh)_2(\mu\text{-}\kappa^2\text{-dppf})]$ (5) in moderate yields, together with small amounts of the corresponding $[Fe_3(CO)_8(\mu_3\text{-}PPh)_2(\kappa^1\text{-}Ph_2PxPPh_2)]$ cluster (x = -C_4H_6-, -C_2H_2-, -C_2H_4-, -C_3H_6-, -$C_5H_4FeC_5H_4$-). The molecular structures of complexes 3 and 5 have been established by X-ray crystallography. Complexes 1–5 have been examined as proton reduction catalysts in the presence of *p*-toluenesulfonic acid (*p*-TsOH) in CH_2Cl_2. Cluster 1 exhibits two one-electron quasi-reversible reduction waves at −1.39 V (ΔE = 195 mV) and at −1.66 V (ΔE = 168 mV; potentials *vs.* Fc^+/Fc). Upon addition of *p*-TsOH the unsubstituted cluster 1 shows a first catalytic wave at −1.57 V and two further proton reduction processes at −1.75 and −2.29 V, each with a good current response. The diphosphine-substituted derivatives of 1 are reduced at more negative potentials than the parent cluster 1. Clusters 2–4 each exhibit an oxidation at *ca.* +0.1 V and a reduction at *ca.* −1.6 V; for 4 conversion to a redox active successor species is seen upon both oxidation and reduction. Clusters 2–4 show catalytic waves in the presence of *p*-TsOH, with cluster 4 exhibiting the highest relative catalytic current ($i^{cat}/i^0 \approx 57$) in the presence of acid, albeit at a new third reduction process not observed for 2 and 3. Addition of the dppf ligand to the parent diphosphinidene cluster 1 gave cluster 5 which exhibited a single reduction process at −1.95 V and three oxidation processes, all at positive values as compared to 2–4. Cluster 5 showed only weak catalytic activity for proton reduction with *p*-TsOH. The bonding in 4 was investigated by DFT calculations, and the nature of the radical anion and dianion is discussed with respect to the electrochemical data.

1. Introduction

Considerable attention has been paid to the fact that hydrogen is a promising energy vector that may function as an alternative to fossil fuels in the future. In nature, hydrogenase enzymes catalyze the reduction of protons to form dihydrogen and/or the oxidation of hydrogen according to the reaction $H_2 \rightleftharpoons 2H^+ + 2e^-$ [1,2]; both the forward and backward reactions are of direct relevance to the use of hydrogen as an energy vector. There are three types of hydrogenases with different metal-containing active sites [3,4], of which the most widely studied are the [Fe-Fe]

☆ Dedicated to Professor Shariff Enamul Kabir on the occasion of this 65th birthday, and in recognition of his outstanding contributions to organometallic chemistry and the development of chemistry in Bangladesh.

* Corresponding authors.
E-mail addresses: ahibur_rahaman@yahoo.com (A. Rahaman), s.colbran@unsw.edu.au (S.B. Colbran), Ebbe.Nordlander@chemphys.lu.se (E. Nordlander).

https://doi.org/10.1016/j.jorganchem.2021.121816

hydrogenases that contain a diiron center supported by CO/CN^- ligands and a dithiolate bridge (the so called H-cluster). This active site is connected through one of the iron atoms, via a bridging cysteinyl sulfur, to an Fe_4S_4 cluster that acts as an electron-donor/acceptor and relays electrons via a chain of closely situated Fe-S clusters [5–7]. A plethora of diiron biomimetics of this active site have been prepared and studied [8–10], and more recently researchers have turned their attention to related tri- and tetra-iron sulfur-containing clusters as potential bioinspired functional proton-reduction catalysts [11,12].

Dinuclear iron complexes with thiolate-, sulfide-, selenide- and telluride bridges have been investigated as electrocatalysts for proton reduction in organic solvents in the presence of suitable proton sources [13–17]. The chemistry of electron-poor diphosphido-bridged diiron carbonyl complexes has been reported [18–27], but only a few diiron diphosphido complexes have been investigated as proton reduction catalysts [28–32].

In a recent study, Colbran and co-workers investigated electrocatalytic proton reduction effected by diiron complexes of the general formula $[Fe_2(CO)_6\{\mu\text{-}P((CH_2\text{-}\eta^5\text{-}C_5H_4)Fe(\eta^5\text{-}C_5H_5))H\}](\eta^5\text{-}C_5H_4)Fe(\eta^5\text{-}C_5H_5)$ = the ferrocenyl radical), derived from the corresponding primary phosphine $P((CH_2\text{-}\eta^5\text{-}C_5H_4)Fe(\eta^5\text{-}C_5H_5))H_2$ [32]. One of the motivations for this work was the desire to incorporate a redox active moiety (a ferrocenyl group) into the ligand(s) in order to emulate the electronic communication between the H-cluster and the iron-sulfur cluster in [FeFe] hydrogenase. It was found that an important aspect of the proton reduction catalyzed by these complexes was the likely formation of hydrogen via the combination of a metal-bound hydride and a bridgehead (phosphido-bound) proton, but that the electrocatalytic behavior was probably not directly dependent on the presence of the potentially redox-active ferrocenyl substituents. In further related studies, we have synthesized and investigated the electrocatalytic proton reduction properties of dinuclear diphosphido-bridged iron clusters where the phosphido and phosphinidene units are derived from the two relatively stable primary phosphines PRH_2 (R = –Ph, 2≠methoxy-1,1≠binaphthyl) [33].

Considering the ability of phosphido-bridged diiron complexes to catalyze proton reduction, we were interested in studying the ability of related iron phosphinidene clusters to function as electrocatalysts for the same reaction. The chemistry of phosphinidene-capped triiron clusters has been relatively thoroughly studied [34–46], but their electrochemical and electrocatalytic behaviors remain relatively poorly investigated. Kochi and co-workers reported the radical anions and dianions of the parent triiron cluster $[Fe_3(CO)_9(\mu_3\text{-}PPh)_2]$ (1) and its derivatives [39,43]. These authors revealed that 1 undergoes successive, reversible, one-electron reductions in THF to produce the anion radical $[1]^{\bullet-}$ and the corresponding dianion $[1]^{2-}$ at the potentials -0.79 and -1.30 V *vs* SCE, respectively, without substantial changes in the cluster framework. The anion radical $[1]^{\bullet-}$ is a labile species that undergoes a series of interesting transformations, especially during electron-transfer catalysis. In a related study, Perkinson *et al.* [41] reported that the diphosphinidene clusters $[Fe_3(CO)_9(\mu_3\text{-}P\text{-}p\text{-}C_6H_4X)(\mu_3\text{-}P\text{-}p\text{-}C_6H_4X')$ (X = X′ = NMe_2, OCH_3, Cl, CF_3, CN)] exhibit two quasi-reversible one-electron reduction processes. However, the electrocatalytic activity of these complexes towards proton reduction has not been investigated. Here we present the synthesis, characterization and electrochemical behavior of $[Fe_3(CO)_9(\mu_3\text{-}PPh)_2]$ (1), and the new electron-rich phosphine derivatives $[Fe_3(CO)_7(\mu_3\text{-}PPh)_2(\kappa^2\text{-}dppb)]$ (2), $[Fe_3(CO)_7(\mu_3\text{-}PPh)_2(\kappa^2\text{-}dppv)]$ (3), $[Fe_3(CO)_7)(\mu_3\text{-}PPh)_2(\kappa^2\text{-}dppe)]$ (4) and $[Fe_3(CO)_7)(\mu_3\text{-}PPh)_2(\mu\text{-}\kappa^2\text{-}dppf)]$ (5). The abilities of clusters 1–5 to act as catalysts for the electrochemical reduction of protons provided from *p*-toluenesulfonic acid (*p*-TsOH) have been studied. In an attempt to crystallize cluster 2, we also obtained the phosphinidene-oxido

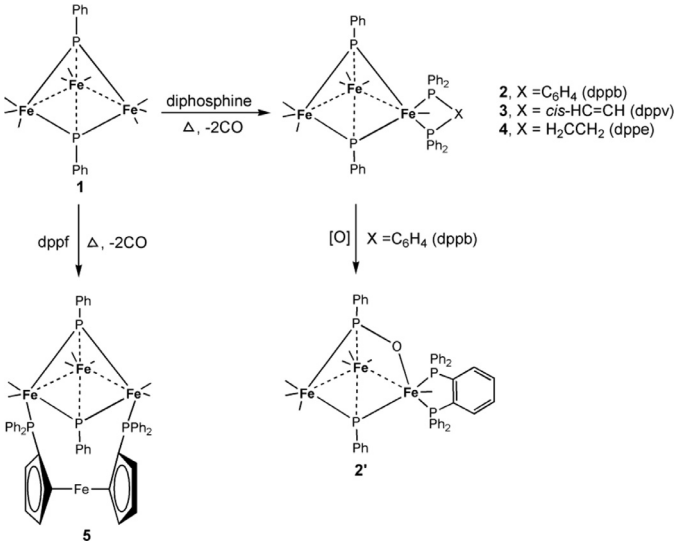

Scheme 1. Schematic depiction of the syntheses of clusters 2–5 from the starting material $[Fe_3(CO)_9(\mu_3\text{-}PPh)_2]$ (1).

derivative $[Fe_3(CO)_7(\mu_3\text{-}PPh)(\mu_3\text{-}\kappa\text{-}O,2,3\text{-}\kappa^2P\text{-}(OPPh)(\kappa^2\text{-}dppb)]$ (2′) (Scheme 1).

2. Experimental

2.1. General procedures

Unless otherwise stated, solvent purification, reactions, and manipulations of compounds were carried out under a nitrogen atmosphere using standard Schlenk techniques. Reagent grade solvents were dried by standard procedures and were freshly distilled prior to use. All chromatographic separations and ensuing work-up were carried out in air. Thin layer chromatography was carried out on glass plates pre-coated with 0.5 mm Merck 60 silica gel. All phosphines were purchased from Acros Organics Chemicals Inc. and used as received. Infrared spectra were recorded on a Nicolet 6700 FT-IR or a Nicolet Avatar 360 FT-IR-spectrometer in solution cells fitted with calcium fluoride or sodium chloride plates; subtraction of the solvent absorptions was achieved by computation. Fast atom bombardment (FAB) mass spectra were obtained on a JEOL SX-102 spectrometer using 3-nitrobenzyl alcohol as matrix and CsI as calibrant. Proton and $^{31}P\{^1H\}$NMR spectra were recorded on a Varian Unity 500 MHz or a Bruker AMX400 spectrometer. The ^1H chemical shifts were referenced to residual solvent resonances, while the ^{31}P chemical shifts were referenced to external 85% H_3PO_4. Elemental analyses were performed by the microanalytical laboratories, University College London.

2.2. Synthesis of $[Fe_3(CO)_9(\mu_3\text{-}PPh)_2]$ (1)

Cluster 1 was synthesized by minor modification of previously reported syntheses [22,33]. A toluene solution (40 mL) of $PPhH_2$ (0.28 ml, 2.5 μmol) was added to iron pentacarbonyl (0.34 ml, 1.7 μmol), and the mixture was heated to 120 °C under a nitrogen atmosphere for 72 h. The solvent was removed under reduced pressure and the residue was chromatographed by TLC on silica gel. Elution with hexane/CH_2Cl_2 (9:1 v/v) gave two bands. The faster moving band gave a small amount of orange microcrystals as a mixture of *anti*/*syn*-$[Fe_2(CO)_6\{(\mu_2\text{-}P(PhH)_2]$ and the second band gave the major product $[Fe_3(CO)_9(\mu_3\text{-}PPh)_2]$(1) (350 mg, 32%) as red crystals after recrystallization from hexane/CH_2Cl_2 at 4 °C. Characterization data for 1: Anal. Calcd for $C_{21}H_{10}Fe_3O_9P_2$:

C, 39.67 H, 1.59 Found: C, 39.85; H, 1.64 %. IR (ν(CO), CH_2Cl_2): 2073 br, 2042 vs, 2021vs, 2003s, 1990 br and 1957 br cm^{-1}. ^1H NMR ($CDCl_3$): δ 7.72 (d, J = 5 Hz, 4H), 7.52 (m, 6H). $^{31}P\{^1H\}$ NMR ($CDCl_3$): δ 318 (s).

2.3. Synthesis of $[Fe_3(CO)_7(\mu_3\text{-}PPh)_2(\kappa^2\text{-}dppb)]$ (2)

A solution of 1 (40 mg, 0.063 mmol) and 1,2-*bis*(diphenylphosphino)benzene (dppb, 28 mg, 0.063 mmol) in THF (20 mL) was refluxed for 12 h. The solvent was removed under reduced pressure and the residue was separated by TLC on silica gel. Elution with *n*-hexane/CH_2Cl_2 (7:3 *v/v*) developed two bands. The faster moving band was unreacted 1 and the second band afforded red microcrystalline $[Fe_3(CO)_7(\mu_3\text{-}PPh)_2(\kappa^2\text{-}dppb)]$ (2) (15 mg, 23%). Characterization data for 2 (2'): Anal. Calc. for $C_{49}H_{34}Fe_3O_6P_4 \cdot 0.5\ CH_2Cl_2$: C, 56.48; H, 3.35. Found: C, 56.55; H, 3.25. IR (ν(CO), CH_2Cl_2): 2040 vs, 1996 vs, 1977 m, 1960 m, 1938 br, 1913 w cm^{-1}. ^1H NMR ($CDCl_3$): δ 7.75 (t, J = 5, 15 Hz, 1H), 7.62 – 7.21 (m, 30H), 7.00 (t, J = 5, 15 Hz, 1H), 6.82 (t, J = 10, 15 Hz, 1H), 6.59 (t, J = 10, 15 Hz, 1H). $^{31}P\{^1H\}$ NMR ($CDCl_3$): δ 401.0 (ddd, J = 20, 123, 141 Hz), 241.3 (ddd, J = 8, 22, 123 Hz), 77.4 (d,d J = 8, 20 Hz), 65.1 (dd, J = 22, 141 Hz). ESI-MS: *m/z* 1042.22 found; *m/z* 1042.25 calc. [M^+] for 2' (1010/1009.93543 for 2). Recrystallization from hexane/CH_2Cl_2 at 4 °C afforded a few red crystals that were shown to be $[Fe_3(CO)_7(\mu_3\text{-}PPh)(\mu_3\text{-}\kappa\text{-}O,2,3\text{-}\kappa^2P\text{-}(OPPh)(\kappa^2\text{-}dppb)]$ (2') by X-ray crystallography (*vide infra*).

2.4. Synthesis of $[Fe_3(CO)_7\ (\mu_3\text{-}PPh)_2(\kappa^2\text{-}dppv)]$ (3)

A solution of 1 (50 mg, 0.078 mmol) and *cis*-1,2-*bis*(diphenylphosphino)ethene (dppv, 31.5 mg, 0.078 mmol) in THF (20 mL) was refluxed for 20 h. The solvent was removed under reduced pressure and the resultant residue was subjected to TLC on silica gel. Elution with n-hexane/CH_2Cl_2 (7:3 v/v) developed one band, which gave $[Fe_3(CO)_7(\mu_3\text{-}PPh)_2(\kappa^2\text{-}dppv)]$ (3) (60 mg, 79%) as deep red crystals after recrystallization from hexane/CH_2Cl_2 at 4 °C. Characterization data for 3: Anal. Calcd for $C_{45}H_{32}Fe_3O_7P_4$: C, 55.37; H, 3.30. Found: C, 55.51; H, 3.37. IR (ν(CO), CH_2Cl_2): 2039 vs, 1995 vs, 1975 m, 1959 m, 1938 br, 1917 w cm^{-1}. ^1H NMR ($CDCl_3$): δ 7.91-7.88 (m, 2H, CH=CH), 7.71 – 6.83 (m, 30H). $^{31}P\{^1H\}$ NMR ($CDCl_3$): δ 402.9 (ddd, J = 18, 111, 145 Hz), 238.4 (ddd, J = 8, 18, 111 Hz), 87.7 (dd J = 8, 18 Hz), 80.4 (dd, J = 18, 145 Hz). ESI-MS: *m/z* 976.28 found; *m/z* 976.16 calc. for [M^+].

2.5. Synthesis of $[Fe_3(CO)_7(\mu_3\text{-}PPh_2)(\kappa^2\text{-}dppe)]$ (4)

A THF solution (20 mL) of 1 (30 mg, 0.0471 mmol) and 1,2-*bis*(diphenylphosphino)ethane (dppe, 18.7 mg, 0.0471 mmol) was refluxed for 12 h. The solvent was removed under reduced pressure and the residue was subjected to thin layer chromatography on silica gel. Elution with n-hexane/CH_2Cl_2 (7:3 v/v) developed two bands. The faster moving band was unreacted 1, the second band afforded $[Fe_3(CO)_7(\mu_3\text{-}PPh)_2(\kappa^2\text{-}dppe)]$ (4) (12 mg, 26%) as red crystals after recrystallization from hexane/CH_2Cl_2 at 4°C. Characterization data for 4: Anal. Calcd for $C_{45}H_{34}Fe_3O_7P_4$: C, 55.25; H, 3.50. Found: C, 55.55; H, 3.65. IR (ν(CO), CH_2Cl_2): 2038 vs, 1995 vs, 1977 m, 1961 m, 1933 br cm^{-1}. ^1H NMR ($CDCl_3$): δ ^1H NMR ($CDCl_3$): δ 7.94 – 6.72 (m, 30H), 2.91-2.68 (m, 2H), 2.52-2.02 (m, 2H). $^{31}P\{^1H\}$ NMR ($CDCl_3$): δ 400.1 (ddd, J = 24, 117, 139 Hz), 240.1 (ddd, J = 10, 22, 117 Hz), 80.2 (dd J = 10, 22 Hz), 63.4 (dd, J = 24, 139 Hz). ESI-MS: *m/z* 978.23 found; *m/z* 978.18 calc. for [M^+].

2.6. Synthesis of $[Fe_3(CO)_7)(\mu_3\text{-}PPh_2)(\kappa^2\text{-}dppf)]$ (5)

A toluene solution (20 mL) of 1 (58 mg, 0.092 mmol), 1,1′-*bis*(diphenylphosphino)ferrocene (dppf, 51 mg, 0.092 mmol) and a solution of Me_3NO (14 mg, 0.182 mmol) in the same solvent (5 ml) was added dropwise through an addition funnel and under nitrogen flow. Upon addition of Me_3NO, the color of the solution gradually turned darker and the reaction mixture was refluxed for 24 h. The solvent was removed under reduced pressure and the residue was subjected to TLC on silica gel. Elution with *n*-hexane/CH_2Cl_2 (7:3 v/v) developed two bands. The faster moving band was unreacted 1, the second band afforded $[Fe_3(CO)_7)(\mu_3\text{-}PPh)_2(\mu\text{-}dppf)]$ (5) (12 mg, 12%) as red crystals after recrystallization from hexane/CH_2Cl_2 at 4 °C. Characterization data for 5: Anal. Calcd for $C_{53}H_{38}Fe_3O_7P_4$: C, 56.15; H, 3.38. Found: C, 56.25; H, 3.26. IR (ν(CO), CH_2Cl_2): 2027 vs, 1990 vs, 1962 m, 1944 w cm^{-1}. ^1H NMR ($CDCl_3$): ^1H NMR ($CDCl_3$): δ 7.80 - 7.40 (m, 20H), 7.14 -7.02 (m, 10H), 4.85 (s, 1H), 4.20 (d, J = 45 Hz, 2H), 3.94 (d, J = 45 Hz, 2H), 3.59 (d, J = 30 Hz, 2H), 3.25 (s, 1H), $^{31}P\{^1H\}$ NMR ($CDCl_3$): 260.2 (t, J = 30, 62 Hz), 66.1 (t, J = 32, 60 Hz) ESI-MS: *m/z* 1134.14; found; *m/z* 1134.28 calc. for [M^+].

2.7. Protonation experiments

Solutions (ca. 1 mL) of the complexes were prepared by dissolving each of complexes 1-5 in CH_2Cl_2 to give solutions with the following concentrations: 3.1 mM (1), 1.9 mM (2), 2.0 mM (3 and 4), 1.8 mM (5) To each solution, two equivalents of *p*-TsOH was added. The acid-containing solution was instantly transferred to an IR cell and monitored over time. The FTIR spectra were unchanged in the presence of acid.

2.8. X-ray structure determinations

Crystals of 1, 2', 3 and 5 suitable for X-ray structure analysis were grown by slow diffusion of hexane into a saturated CH_2Cl_2 solution at 4 °C. Crystals were immersed in cryo-oil, mounted in a Nylon loop, and measured at a temperature of 120-170 K. The X-ray diffraction data were collected on a Bruker Kappa Apex II Duo or an Agilent Supernova diffractometer using Mo Kα radiation (λ = 0.71073 Å). The APEX2 [47] or CrysAlisPro [48] program packages were used for cell refinements and data reductions. Structures were solved by direct methods or by charge flipping using the SHELXS-97 [49] or SUPERFLIP [50] programs. A multi-scan, numerical, or Gaussian absorption correction (SADABS [51] or CrysAlisPro [48]) was applied to all data. The solvent of crystallization (CH_2Cl_2) in 2' was slightly disordered. No stable disorder model could be obtained without strict geometric restraints. Therefore, no disorder model was used, but the chloride atoms were restrained so that their U_{ij} components approximate isotropic behavior. Structural refinements were carried out using SHELXL-97 or SHELXL-2013 [49]. The hydrogen atoms were positioned geometrically and constrained to ride on their parent atoms, with C-H = 0.95–0.99 Å and U_{iso} = 1.2 U_{eq}(parent atom). Crystallographic details are summarized in Table S1 (Supplementary Material).

2.9. Electrochemistry

Cyclic voltammetry experiments were carried out at room temperature in deoxygenated CH_2Cl_2 or acetonitrile solutions with 0.1 M [NBu_4][PF_6] as the supporting electrolyte. The working electrode was a 3 mm diameter glassy carbon electrode that was polished with 0.3 μm alumina slurry, then washed with the solvent, prior to each scan. The counter electrode was a platinum wire and a silver wire was employed as a quasi-reference electrode. All potentials were referenced to the ferrocenium/ferrocene (Fc^+/Fc) redox

couple measured *in situ* at the end of each experiment. A Pine WaveNow potentiostat was used for all electrochemical measurements. Studies of electrocatalytic proton reduction were carried out by adding equivalents of *p*-TsOH. Analyte concentrations and scan rates are given in the caption to each relevant figure (*vide infra*).

2.10. Computational methodology

All calculations were performed with the hybrid meta exchange-correlation functional M06 [52], as implemented by the Gaussian 09 program package [53]. The iron atoms were described by Stuttgart-Dresden effective core potentials (ECP) and an SDD basis set [54], while a 6-31G(d') basis set was employed for the remaining atoms [55]. The ancillary phenyl groups were replaced with methyl groups for computational expediency, and Grimme's dispersion correction was included in all optimizations [56].

The optimized structures represent a ground-state minimum based on the Hessian matrix that displayed only positive eigenvalues. The natural charges (*Q*) and Wiberg bond indices were computed using Weinhold's natural bond orbital (NBO) program (version 3.1) [57,58]. The geometry-optimized structures presented here have been drawn with the JIMP2 molecular visualization and manipulation program [59].

3. Results and discussion

3.1. Synthesis and characterization

Heating of THF solutions of $[Fe_3(CO)_9(\mu_3\text{-PPh})_2]$ (1) with the diphosphines, dppb, dppv or dppe for 12-20 h gave the complexes $[Fe_3(CO)_7(\mu_3\text{-PPh})_2(\kappa^2\text{-dppb})]$ (2), $[Fe_3(CO)_7(\mu_3\text{-PPh})_2(\kappa^2\text{-dppv})]$ (3) and $[Fe_3(CO)_7)(\mu_3\text{-PPh})_2(\kappa^2\text{-dppe})]$ (4) in moderate to good yields (12–79%). Complexes 2, 3 and 4 were characterized by elemental analysis, mass spectrometry, and by IR, ^{1}H and $^{31}P\{^1H\}$ NMR spectroscopy, and, in the case of 3, X-ray crystallography. Attempts to crystallize 2 gave the oxygenated derivative $[Fe_3(CO)_7(\mu_3\text{-PPh})(\mu_3\text{-}\kappa^1\text{-O,2,3-}\kappa^2\text{P-(OPPh)}(\kappa^2\text{-dppb})]$ (2') (*vide infra*). The complexes show $\nu_{(C\text{-}O)}$ bands in the region 2038–1913 cm^{-1}, consistent with all terminal carbonyl groups. Shifts to lower $\nu_{(C\text{-}O)}$ frequencies by approximately 35–60 cm^{-1} were observed upon substitution of carbonyl ligands in 1 by the diphosphines to afford 2, 3, and 4, consistent with the buildup of electron density on the iron centres in the $Fe_3(CO)_x$ core. The $^{31}P\{^1H\}$ NMR spectra of clusters 2-4 exhibit two phosphinidene multiplets and two phosphine multiplets at similar shifts for all three molecules, consistent with their proposed asymmetric structures.

Treatment of 1 with dppf and two equivalents of trimethyl amine-*N*-oxide in toluene afforded $[Fe_3(CO)_7(\mu_3\text{-PPh})_2(\mu\text{-dppf})]$ (5) as the major product. Complex 5 was fully characterized by a combination of elemental analysis, mass spectrometry, and by IR, ^{1}H NMR, $^{31}P\{^1H\}$ NMR spectroscopy data together with a single crystal X-ray diffraction study. The IR spectrum of 5 exhibits carbonyl bands in the 2027–1944 cm^{-1} region, consistent with all carbonyl ligands being terminally bonded. The ^{1}H NMR spectrum of the complex reveals peaks in the aromatic region for the phenyl protons, and the $^{31}P\{^1H\}$ NMR spectrum displays a triplet at δ 260.2 for two equivalent phosphinidene P-atoms and a triplet at δ 66.1 for two equivalent dppf phosphorus atoms, which is indicative of a symmetric structure where the dppf ligand bridges the nonbonded Fe-Fe "edge", as depicted in Scheme 1 (*vide supra*). As the dppf ligand is not expected to lie "in plane" with the triiron moiety, a C_2 symmetry is expected for the molecule (*vide infra*). There is a possibility of libration (torsional rotation around the axis passing through the cyclopentadienyl ring centroids) and inversion of the dppf ligand axis with respect to the triiron core (leading to a chemically and magnetically equivalent enantiomeric C_2 structure). Such libration/fluxionality has been studied previously for trinuclear carbonyl clusters of the iron triad [60], but was not studied here.

3.2. Structural studies

The relative orientation of the phosphinidene bridgehead groups and the chelating diphosphine ligand could not be unambiguously determined on the basis of the IR and NMR spectroscopic studies. Thus, crystallographic studies were carried out on clusters 1, 2', 3 and 5. The crystal and structure solution data are summarized in the supporting information (Table S1). Salient bond length and angle data are presented in the Figure captions. The crystal structure of 1 has been reported previously [46] and a view of the molecular structure is shown in the supporting information (Figure S1). The metric parameters for the triiron cluster are very similar to those previously reported [46] and are not discussed further here.

The molecular structure of the unusual complex 2' consists of an approximately equatorial triiron core with two Fe–Fe bonds and one open edge (Figure. S2). The triiron unit is capped by the mutual *anti* relationship of a triply bridging μ_3-PPh ligand and one phosphinidene-oxido (κ^1-O,κ^2P-(OPPh)) ligand. The origin of the oxygen atom that has been inserted into a metal-phosphorus bond to form 2' is unclear; it may derive from (partially) oxidized primary phosphine or the presence of adventitious water. We have previously observed the insertion of an oxygen atom into a metal-phosphorus bond in the case of a chelating diphosphine derivative of $[H_4Ru_4(CO)_{12}]$, *viz.* 1,1-$[H_4Ru_4(CO)_{10}$-(O-DUPHOS)] (DUPHOS = (-)-1,2-Bis[(2*R*,5*R*)-2,5-dimethylphospholano]benzene [61]). Furthermore, Shi *et al.* observed the insertion of oxygen into a phosphido-metal bond in the complex $[Fe_2(\mu\text{-}PPh_2)_2(CO)_6]$ [31] and found that this could be suppressed by the rigorous exclusion of dioxygen and water.

The molecular structures of complexes 3 and 5 (Figs. 1 and 2, respectively) comprise an open triangular triiron core, *i.e.*, two Fe–Fe bonds, spanned by two triply bridging (capping) phenyl phosphinidene groups, one 'above' and one 'below' the triiron plane. In complexes 2' and 3, the bidentate diphosphine ligand (dppb and dppv, respectively) chelates to a single iron atom, while in 5, the dppf ligand spans an Fe–Fe edge, and the structure confirms the expected C_2 symmetry of the molecule. For complexes 2' and 3, the chelating diphosphine ligand occupies two axial positions non-coplanar with the iron triangle; this also appears to be the conformation in solution as suggested by the ^{31}P NMR spectra of the two complexes. For 2' and 3, the metal-metal distances that involve the central iron atom and that which is coordinated by the diphosphine (Fe1–Fe2) are larger (for 2'; Fe1–Fe2 = 2.8445(6) Å; 3: Fe1–Fe2 = 2.8525(3) Å) than in the parent cluster 1 (Fe–Fe_{av} = 2.7186(4), while the other iron-iron edge is shorter than than the parent cluster 1 (2': Fe2–Fe3 = 2.6541(6) Å; 3: Fe2–Fe3 = 2.6849(4) Å). The reason for these changes in bond distances is most likely the electronic influence of the ligands. The phosphine moieties are not as good π-acceptors as carbonyl ligands. Therefore, buildup of electron density on the phosphine-substituted iron (Fe1 for both 2' and 3) means that there is less need for a strong FeFe interaction with the central iron atom (Fe2 for both clusters); this is in turn compensated by a stronger interaction between Fe2 and Fe3. The Fe–Fe–Fe bond angles are 87.384(18), 80.06(9), and 86.758(11) deg. for 2', 3 and 5, respectively, which are comparable to 81.087(13) deg. for the parent cluster 1 and to 81.0(3) deg. for the structurally analogous cluster $[Fe_3(CO)_9(\mu_3\text{-S})_2]$ [62]. The diphosphine P1–Fe–P2 bite angles are 87.15(3) and 85.450(16) deg. for 2' and 3, respectively, which are very similar to the corresponding angles in the structurally

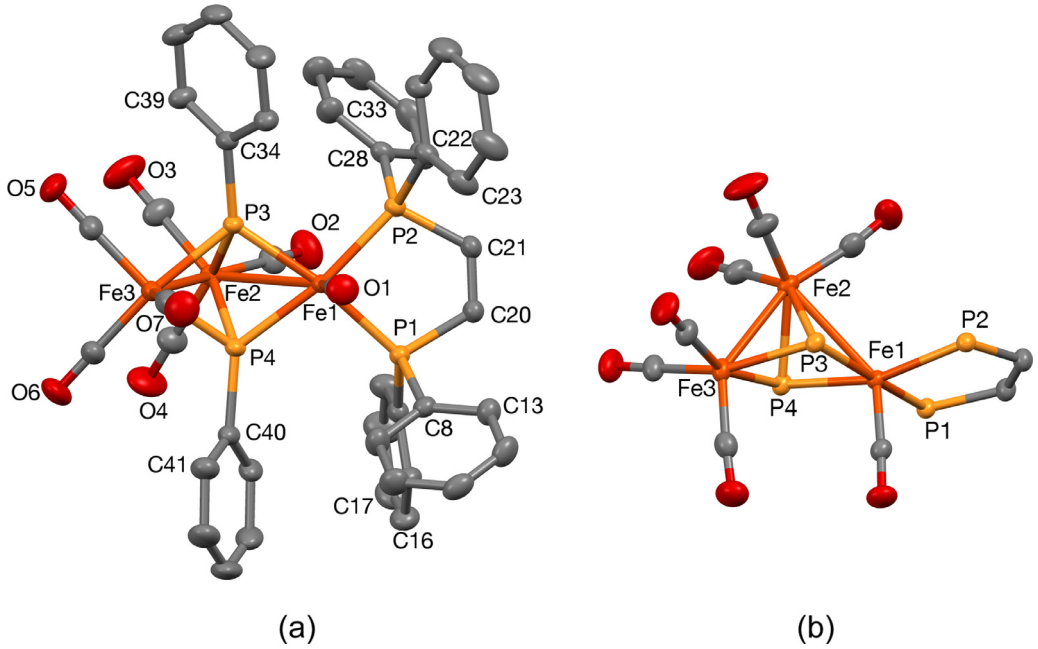

Fig. 1. (a) Molecular structure of $[Fe_3(CO)_7(\mu_3\text{-}PPh)_2(\kappa^2\text{-}dppv)]$ (3) with selected bond lengths (Å) and angles (°); showing the atom numbering scheme. Thermal ellipsoids are drawn at the 50% probability level and the hydrogen atoms are omitted for clarity. Key bond length and angle data: Fe(1)-P(3) 2.1960(4), Fe(1)-P(4) 2.2095(4), Fe(1)-P(1) 2.2466(4), Fe(1)-P(2) 2.2590(5), Fe(1)-Fe(2) 2.8525(3), Fe(2)-C(3) 1.7829(19), Fe(2)-C(2), 1.783(2) Fe(2)-C(4) 1.7880(19), Fe(2)-P(3) 2.2429(5), Fe(2)-P(4) 2.2543(5), Fe(2)-Fe(3) 2.6849(4), Fe(3)-C(7) 1.773(2), Fe(3)-C(6) 1.8026(18), Fe(3)-C(5) 1.8033(18), Fe(3)-P(4) 2.2145(5), Fe(3)-P(3) 2.2203(5), P(3)-Fe(1)-P(4) 70.960(16), P(1)-Fe(1)-P(2) 85.450(16), P(4)-Fe(1)-Fe(2) 50.978(12), Fe(3)-Fe(2)-Fe(1) 80.068(9), Fe(1)-P(3)-Fe(3) 107.614(17), Fe(1)-P(3)-Fe(2) 79.965(16), Fe(3)-P(3)-Fe(2) 73.963(15), Fe(1)-P(4)-Fe(3) 107.342(18), Fe(1)-P(4)-Fe(2) 79.429(16), Fe(3)-P(4)-Fe(2) 73.849(15). (b) A plot of the essential metal-ligand framework of 3; note that the orientation is different from that in (a).

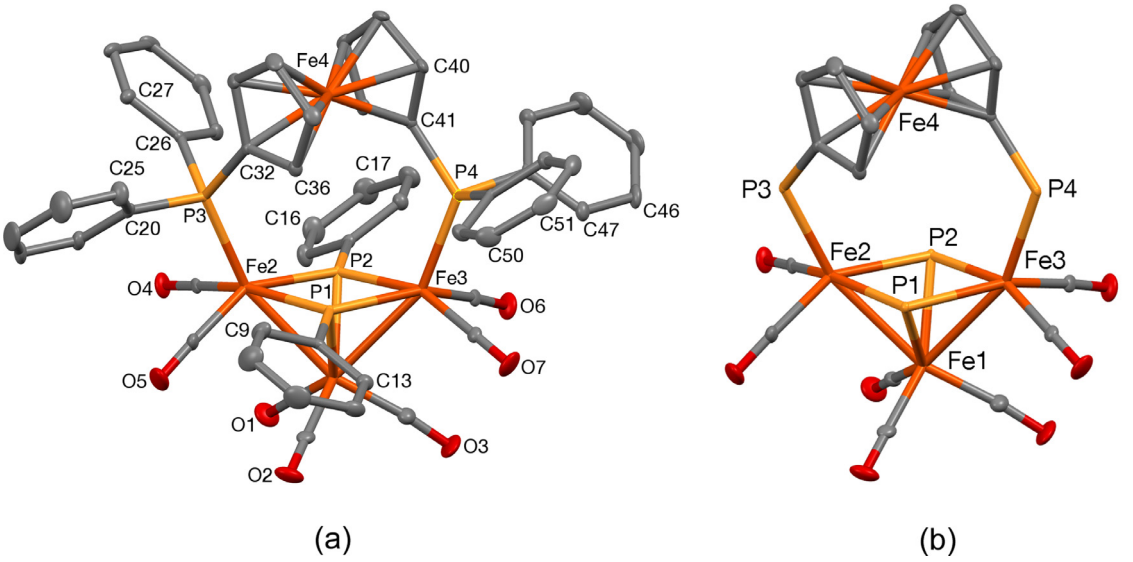

Fig. 2. (a) Molecular structure of $[Fe_3(CO)_7](\mu_3\text{-}PPh)_2(\mu\text{-}dppf)]$ (5) with selected bond lengths (Å) and angles (°); and showing the atom numbering scheme. Thermal ellipsoids are drawn at the 50% probability level. The hydrogen atoms are omitted for clarity: Fe(1)-P(2) 2.2818(5), Fe(1)-P(1) 2.2789(5), Fe(2)-P(1) 2.2352(5), Fe(2)-P(2) 2.2358(5), Fe(1)-Fe(2) 2.6641(4), Fe(3)-P(1) 2.2435(5), Fe(3)-P(2) 2.2307(5), Fe(2)-Fe(3) 2.6704(4), Fe(3)-P(4) 2.2225(5), Fe(3)-P(3) 2.2203(5), P(1)-Fe(1)-P(2) 68.388(16), P(2)-Fe(3)-P(1) 69.899(17), P(2)-Fe(1)-Fe(2) 53.069(13), Fe(3)-Fe(1)-Fe(2) 86.758(11), Fe(3)-P(2)-Fe(2) 110.23(2), Fe(1)-P(1)-Fe(2) 72.331(16), Fe(3)-P(1)-Fe(2) 109.78(2), Fe(1)-P(1)-Fe(3) 72.377(15), Fe(1)-P(2)-Fe(3) 72.557(15), P(1)-Fe(1)-Fe(2) 53.075(13). (b) A plot of the essential metal-ligand framework of 5.

analogous cluster $[Fe_3S_2(CO)_5(dppv)_2]$ [44]. The Fe–$P_{phosphine}$ bond distances are comparable to those observed for the same ligands in related clusters, *e.g.*, $[Fe_3S_2(CO)_5(dppv)_2]$ [44] and $[Fe_3(CO)_5(\mu\text{-}edt)_2(\kappa^2\text{-}dppv)]$ (edt = 1,2-ethanedithiol) [12a].

The bonding in cluster 4 was investigated by electronic structure calculations. Here we optimized the structure of $[Fe_3(CO)_7(\mu_3\text{-}PMe)_2(\kappa^2\text{-}dppe\text{-}Me_4)]$, whose DFT structure (**A**) appears in the supporting information (Figure S3). Species **A** is similar in nature to the solid-state structure of cluster 3 with the Fe–Fe bond containing the chelating disphosphine ligand 0.062 Å longer than the other Fe-Fe bond, whose distance is 2.667 Å. The non-bonding distance between the two wing-tip iron centers is 3.568 Å, and this is in good agreement with the corresponding non-bonding Fe–Fe distance found in clusters 1, 3, and 5. Table S2 in the supporting information reports selected Natural charges (*Q*) [63], bond distances, and Wiberg bond indices (WBIs) [64] in **A**. The WBIs for the two Fe–Fe bonds are 0.28 and 0.33, and the smaller WBI corresponds to the Fe—Fe bond containing the chelating diphosphine ligand. A

Table 1
Summary of electrochemical data from cyclic voltammetry of complexes 1–5.

Complex	Reduction processes $E_{1/2}$/V vs $Fc^{+/0}$ (ΔE_p/mV)	Oxidation processes $E_{1/2}$/V vs $Fc^{+/0}$ (ΔE_p/mV)
$[Fe_3(CO)_9(\mu_3\text{-PPh})_2]$ (1)	−1.39 (195) −1.66 (168)	–
$[Fe_3(CO)_7(\mu_3\text{-PPh})_2(\kappa^2\text{-dppb})]$ (2)	−1.57 (395)	+0.11 (259)
$[Fe_3(CO)_7(\mu_3\text{-PPh})_2((\kappa^2\text{-dppv})]$ (3)	−1.57 (425)	+0.12 (409)
$[Fe_3(CO)_7)(\mu_3\text{-PPh})_2(\kappa^2\text{-dppe})]$ (4)	−1.55 (199) [a] −1.88 (160)	+0.08 (159) [a] +0.36 (169)[a]
$[Fe_3(CO)_7)(\mu_3\text{-PPh})_2(\mu\text{-}\kappa^2\text{-dppf})]$ (5)	−1.89 (130)	+0.23 (130) +0.54 (159) +0.93 (130)

[a] Not a fully chemically reversible process ($i^{reverse}/i^{forward} < 1.0$).

WBI of 0.05 was computed for the wingtip irons, supporting the absence of any significant bonding interaction between these iron centers.

The composition of the HOMO and LUMO in species **A** was also examined, and these orbitals are depicted in Figure S1. The HOMO exhibits significant in-phase bonding between the iron centers involved with the pair of Fe–Fe bonds. One-electron oxidation of the cluster (*i.e.* removal of a bonding electron from the HOMO) is expected to weaken the bonding within of the $Fe_3(PMe)_2$ cluster core thereby promoting possible rearrangement. The orbital interaction between the non-bonded wingtip iron centers is clearly antibonding in nature and in keeping with the observed *nido* polyhedron found in this genre of trimetallic clusters. The LUMO is composed of antibonding Fe–Fe bonds that are also antibonding with respect to the capping phosphinidene ligands. Electron addition to the LUMO is expected to promote the expansion, and possibly scission, of the Fe–Fe(CO)(PP) bond (where PP = κ^2-dppe-Me_4) within the cluster. One-electron oxidation of the cluster (i.e. removal of a bonding electron from the HOMO) is expected to weaken the bonding within the $Fe_3(PMe)_2$ cluster core, thereby promoting possible rearrangement. The cyclic voltammetry of cluster 4 support the proposed rearrangement of the cluster following both one-electron reduction and one-electron oxidation (*vide infra*).

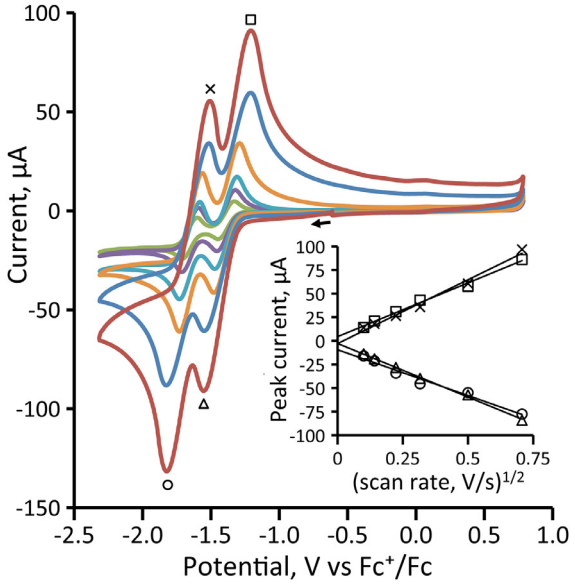

Fig. 3. CVs of $[Fe_3(CO)_9(\mu_3\text{-PPh})_2]$ (1, 2 mM) in dichloromethane - 0.1M $[NBu_4][PF_6]$ at scan rates 10, 25, 50, 100, 250, 500 mV s^{-1} recorded at a glassy carbon working electrode. Potentials are relative to the ferrocene-ferrocenium couple. The inset shows a plot of peak current *vs* square root of scan rate and the equal forward and reverse currents indicate chemical reversibility for the reductions.

3.3. Electrochemical studies

The cyclic voltammetry of complexes 1–5 was investigated, primarily to determine reduction potentials that might be related to electrocatalytic proton reduction activity (*vide infra*). Dichloromethane was used as the primary solvent for these studies because dichloromethane is an innocent solvent in the context of electrochemistry of metal carbonyl complexes. In the following commentary, all potential data, including peak-to-peak separations for couples, is taken from cyclic voltammograms at scan rate 100 mV s^{-1} and is referenced against the Fc/Fc^+ couple. The potentials of the important redox processes observed in the cyclic voltammograms are summarized in Table 1.

The electrochemistry of $[Fe_3(CO)_9(\mu_3\text{-PPh})_2]$ (1) was investigated in CH_2Cl_2, and also in THF. Very similar electrochemical behaviours for 1 were observed in both solvents. In CH_2Cl_2, cluster 1 exhibited two quasi-reversible, one-electron reduction processes at −1.39 V (ΔE_p = 195 mV) and at −1.66 V (ΔE_p = 168 mV) (Fig. 3). Plots of the peak currents against $v^{1/2}$ are linear (see the insets in Fig. 4) in accord with the Randles-Sevcik equation and indicate that all redox processes are for species freely diffusing in solution. This compares well with the behaviour observed by Ohst and Kochi for the same complex [43]. Similarly, Perkinson *et al.* [41] have reported that the clusters $[Fe_3(CO)_9(\mu_3\text{-P-}p\text{-}C_6H_4X)(\mu_3\text{-P-}p\text{-}C_6H_4X')$ (X = X′ = NMe_2, OCH_3, Cl, CF_3, CN)] exhibited two quasi-reversible one-electron reduction processes. We have observed the same behavior in cluster $[Fe_3(CO)_9(\mu_3\text{-Te})_2]$ [65], which shows two quasi-reversible one-electron reduction processes at −0.97 V (ΔE_p = 155 mV) and −1.51 V (ΔE_p = 145 mV), significantly less negative than cluster 1 in CH_2Cl_2.

The electrochemical properties of the diphosphine-substituted clusters 2 and 3 were investigated in CH_2Cl_2. Clusters 2 and 3 (Fig. 4) each exhibit one quasi-reversible oxidation, at +0.11 (ΔE_p = 259 mV) and +0.12 (ΔE_p = 409 mV), respectively, and one quasi-reversible reduction at −1.57 (ΔE_p = 395 mV) and −1.57 (ΔE_p = 425 mV), respectively. No additional features were observed in the CVs from −2.5 to +1.0 V. Addition of the diphosphine ligand in clusters 2 and 3 not only results in shifting of the reduction potentials to more negative values compared to 1, but now oxidative chemistry is seen within the solvent window. These observations are consistent with the increasing electron density within the cluster cores of 2 and 3 compared to the parent cluster 1 (*cf.* discussion above).

Surprisingly, the electrochemistry of cluster 4 is more complex than that of clusters 1–3. CVs of 4 to positive potentials exhibit a quasi-reversible primary oxidation couple at +0.08 V (ΔE_p = 155 mV) followed by a second oxidation couple at +0.36 V, which diminishes in current relative to the primary oxidation process with increasing scan rate (Fig. 5). To negative potentials, the CVs of cluster 4 reveal a quasi-reversible primary reduction couple at −1.55 V followed by a second reduction couple at −1.88 V,

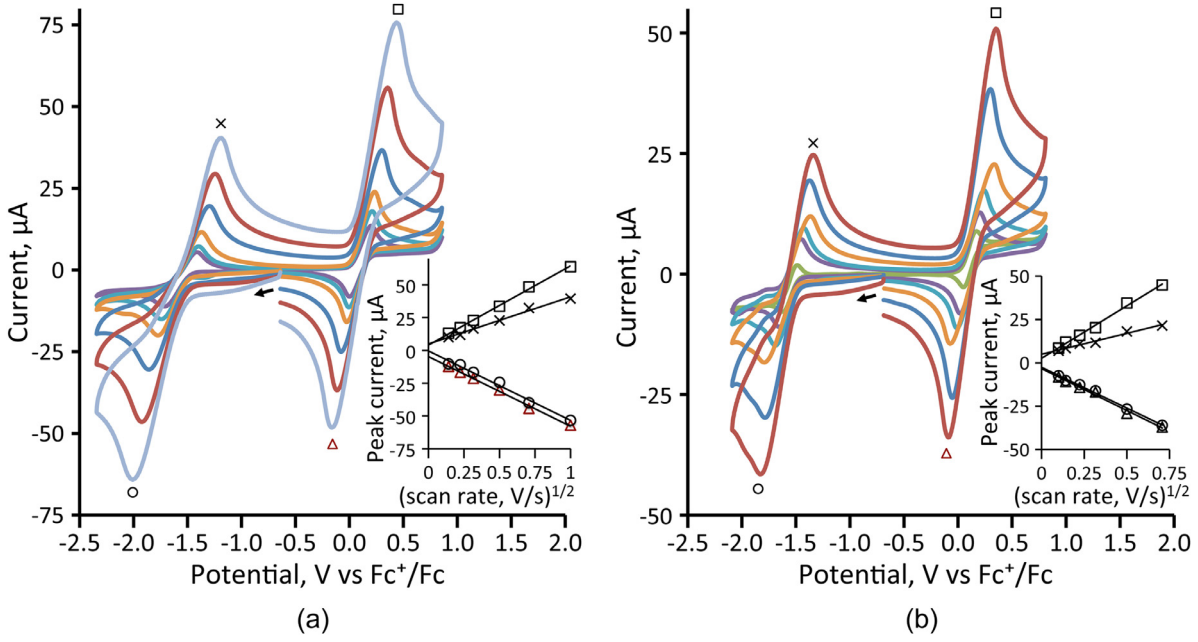

Fig. 4. CVs of (a) $[Fe_3(CO)_7(\mu_3\text{-PPh})_2(\kappa^2\text{-dppb})]$ (2, 2 mM)) with scan rates 25, 50, 100, 250, 500, 1000 mV s^{-1} and (b) $[Fe_3(CO)_7\{(\mu_3\text{-PPh}\}_2(\kappa^2\text{-dppv})]$ (3, 2 mM) with scan rates 10, 25, 50, 100, 250, 500 mV s^{-1}; other conditions as for Fig. 4. The insets show a plot of peak current *vs* square root of scan rate, and the unequal forward and reverse currents and magnitudes of the plot slopes indicate less chemical reversibility for the reduction.

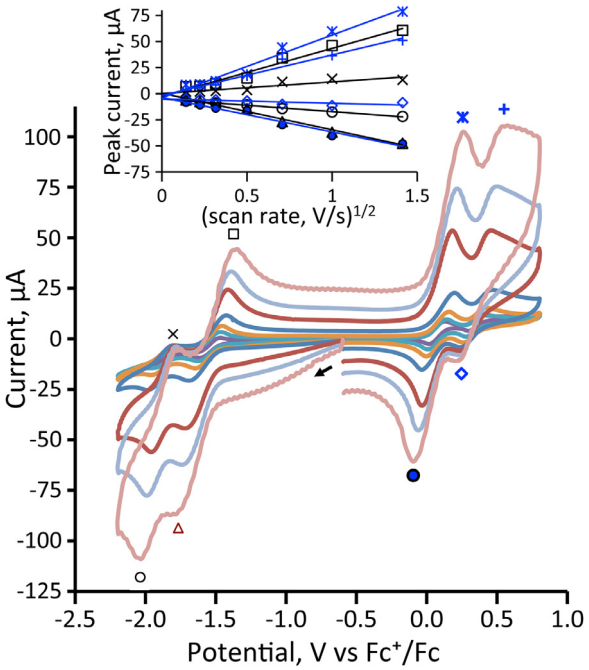

Fig. 5. CVs of $[Fe_3(CO)_7\{(\mu_3\text{-PPh}\}_2(\kappa^2\text{-dppe})]$ (4) (2mM) with scan rate 25, 50, 100, 250, 500, 1000, 2000 mV s^{-1}; other conditions as for Fig. 4. The insets show a plot of peak current *vs* square root of scan rate and the forward and reverse currents indicate less chemical reversibility for the second reduction and the second oxidation.

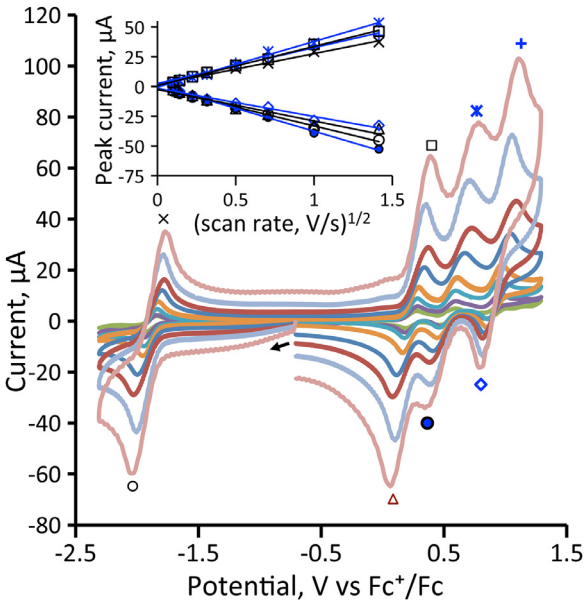

Fig. 6. CVs of $[Fe_3(CO)_7\{(\mu_3\text{-PPh}\}_2(\mu\text{-dppf})]$ (5) (2mM) with scan rate 10, 25, 50, 100, 250, 500, 1000, 2000 mV s^{-1}; other conditions as for Fig. 4. The inset shows a plot of peak current *vs* square root of scan rate and the equal forward and reverse currents indicate chemical reversibility for the reduction and oxidations.

which loses current relative to the primary reduction current as the scan rate increases. The current dependencies of the secondary reduction and oxidation couples with scan rate indicate that these processes arise from species produced by a chemical step following the reduction and the oxidation of 4, respectively (at faster scan rates there is less time for the chemical step to occur). Rearrangements of cluster 4 upon both reduction and oxidation are supported by the DFT computational results; the nature of the reduced forms of 4 is discussed below.

The cyclic voltammogram of the diphosphinoferrocene-substituted triiron cluster 5 showed three consecutive quasi-reversible oxidation waves at +0.23 (ΔE_p = 130 mV), +0.54 (ΔE_p = 159 mV) and +0.93 V (ΔE_p = 120 mV) and one quasi-reversible reduction wave at −1.89 V (ΔE_p = 130 mV) (Fig. 6). Substitution of the diphosphinoferrocene, dppf, ligand at the base of the triiron cluster not only results in the first reduction potential shifting to more negative values compared to 1–4, but three oxidation couples appear within the solvent window. The first and

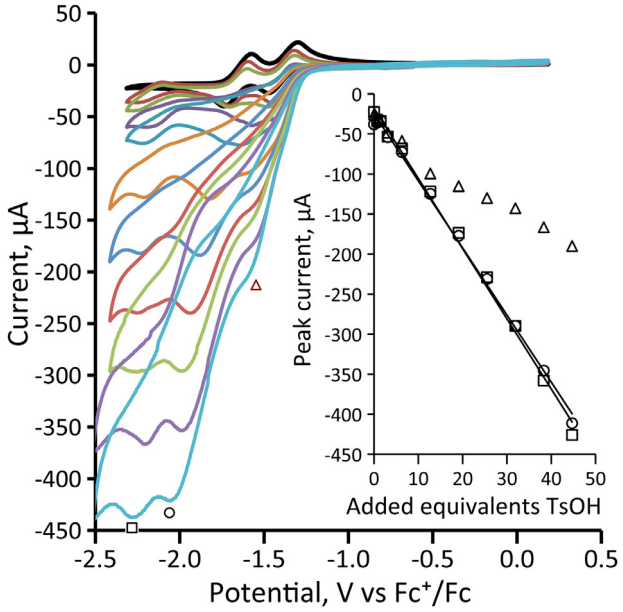

Fig. 7. CVs of complex $[Fe_3(CO)_9(\mu_3\text{-PPh})_2]$ (1) (2 mM) in CH_2Cl_2-0.1 M $[NBu_4][PF_6]$ in the absence and presence of up to 45 molar equivalents of *p*-TsOH; scan rate 0.50 Vs^{-1}, 3.0 mm diameter minidisk glassy carbon working electrode, potential relative to the ferrocene/ferrocenium couple. See Supplementary Information for an MPEG4 movie of the electrochemical response for 1 during proton reduction.

last oxidation couples can be attributed to oxidation of the triiron centre as the middle couple at +0.54 V is almost certainly the $Fe^{II/III}$ couple of the ferrocene core of the coordinated dppf ligand. The unreacted, free, dppf ligand shows an irreversible oxidation at +0.20 V, which becomes reversible and shifts to more positive potential at *ca.* +0.5–0.69 V when coordinated to a metal center [66]. The chemical reversibility of the oxidation and reduction couples was unchanged at all scan rates.

3.4. Electrocatalytic studies

A qualitative survey of the electrocatalytic activity of each complex towards proton reduction was performed by cyclic voltammetry in the presence of *p*-TsOH. As the pK_a of *p*-TsOH in dichloromethane is unknown and only quasi-reversible electrochemical responses were observed for the clusters, quantitative analyses of the proton reduction activity is not possible. In all cases, blank runs of *p*-TsOH at the highest concentration used were made (*cf.* Supplementary Material, Figures S4-S8). In all blank runs, a small negative peak at *ca* –2.4 V was observed, and this reductive peak may be assumed to contribute to any reductive waves at potentials lower –2.2 V, complicating any analysis of current response at such negative potentials. A comparison between clusters 1–5 is indicative of their relative activity.

Fig. 8 depicts the complicated response that was observed in CVs of $[Fe_3(CO)_9(\mu_3\text{-PPh})_2]$ (1) in the presence of *p*-TsOH. Beyond three molar equivalents of acid added to 1, four successive waves for catalytic reduction of protons are observed in the reductive region. As increasing amounts of *p*-TsOH were added: (*i*) the reversibility of the first and second reductions was lost; (*ii*) the cathodic currents of the first and second reduction couples (labelled Δ and × in Fig. 7, respectively) increased concomitant with (*iii*) a loss of reversibility and (*iv*) a shift to higher potential; (*v*) two new peaks with high cathodic current (labelled Δ and ∘ in Fig. 7) appear. Of note, the first catalytic reduction appears at –1.57 V, which is a less negative potential than those observed for the diphosphine-triiron cluster derivatives to be described next. With increasing acid concentration, the second and third catalytic reduction waves increased in current and shifted to more negative potential. Limiting catalytic currents were not reached with the maximum *p*-TsOH (45 equiv.) used.

Kochi and co-workers have reported that the protonation of the dianion 1^{2-} occurs directly at the phosphinidene cap(s) and leads to the formation of $[Fe_3(CO)_9(\mu_3\text{-PPh})(\mu_2\text{-PPhH})]^-$ at –78 °C [43]. Upon addition of up to 45 equivalents of acid, the first and second reduction did not show a positive shift in potential. A shift of these reductions in the positive direction would have been expected in the event that either of the species being reduced was protonated prior to reduction. The observed electrochemical response is suggestive of the first and second catalytic proton reduction steps involving formation of the monoanion 1^- and the dianion 1^{2-}, respectively. Most probably subsequent protonation occurs, initially leading to formation of $[Fe_3(CO)_9(\mu_3\text{-PPh})(\mu_2\text{-PPhH})]^\bullet$ or of $[Fe_3(CO)_9(\mu_3\text{-PPh})(\mu_2\text{-PPhH})]^-$, respectively, and subsequent spontaneous electrochemical reduction of the protonated species, protonation again, and reductive elimination (of hydrogen) steps would then lead to hydrogen evolution and regeneration of the catalytically active 1^- and/or 1^{2-} anions.

The ability of clusters 2 and 3 to act as proton reduction catalysts was assayed next (Fig. 8). Both clusters show similar electrochemical responses to increasing amounts of acid (*p*-TsOH). As the acid concentration increased, the reduction couple lost chemical reversibility within the addition of one equivalent of acid and, with increasing acid, gave rise to a catalytic wave for proton reduction at *ca.* –1.84 V for 2 and at –1.75 V for 3. The catalytic wave reached a limiting current ratio of $i_p^{cat}/i_p^0 \approx 10$ at *ca.* 32 equivalents of *p*-TsOH for 2 and of $i_p^{cat}/i_p^0 \approx 9$ at *ca.* 13 equivalents of *p*-TsOH for 3. A second catalytic wave appears with increasing acid concentration, at *ca* –2.1 V for 2 and at *ca.* –2.0 V for 3, which shows a strong shift to negative potential with increasing acid concentration such that it moves out of the CV window at the highest acid concentrations employed (see Fig. 8); an improved electrochemical response is observed at these higher acid concentrations due to better activation of the working electrode. The oxidation couples of 2 and 3 sharpen, but are otherwise unperturbed, with increasing amounts of acid. The sharpened response is again consistent with better activation of the glassy carbon electrode with higher concentrations of acid.

The electrochemical behaviour of 4 with increasing equivalents of *p*-TsOH was also examined (Fig. 9). As increasing amounts of *p*-TsOH were added, the cathodic currents of the first and second reduction couples increased, consistent with proton reduction catalysis. Current maxima were reached with $i_p^{cat}/i_p^0 \approx 3$ at *ca.* six equivalents of *p*-TsOH and $i_p^{cat}/i_p^0 \approx 20$ at *ca* 32 equivalents *p*-TsOH for the first and second catalytic waves (labelled Δ and ∘ in Fig. 9), respectively. Beyond 13 equivalents of added *p*-TsOH, a new process (labelled □ in Fig. 9) grows in and rapidly dominates the catalytic wave(s) for proton reduction. The reduction potential of the new (third) reduction process moves more negative with increasing *p*-TsOH concentration and gives $i_p^{cat}/i_p^0 \approx 57$ at 45 equivalents *p*-TsOH. This relative catalytic current is the highest observed for clusters 1–5 and, therefore, cluster 4 is the most active of these catalysts in terms of rate.

The observation of increasing catalytic currents for proton reduction at the first and second reductions of 4 as increasing *p*-TsOH is added indicates that both $4^{\bullet-}$ and 4^{*2-} (the reduction product of the species (4^{*-}) formed by the chemical step that follows formation of $4^{\bullet-}$; *vide supra*), are catalytically competent species. However, the rates of catalysis by both $4^{\bullet-}$ and 4^{*2-} saturate at low equivalents of *p*-TsOH (by 6 and 32 equiv., respectively; see above). Beyond 13 equiv. of *p*-TsOH, the newly appeared, third reduction potential revealed at ca. –2.07 V relates to the process that dominates the current for proton reduction. The requirement for a large excess of acid and the prior formation of the dianion

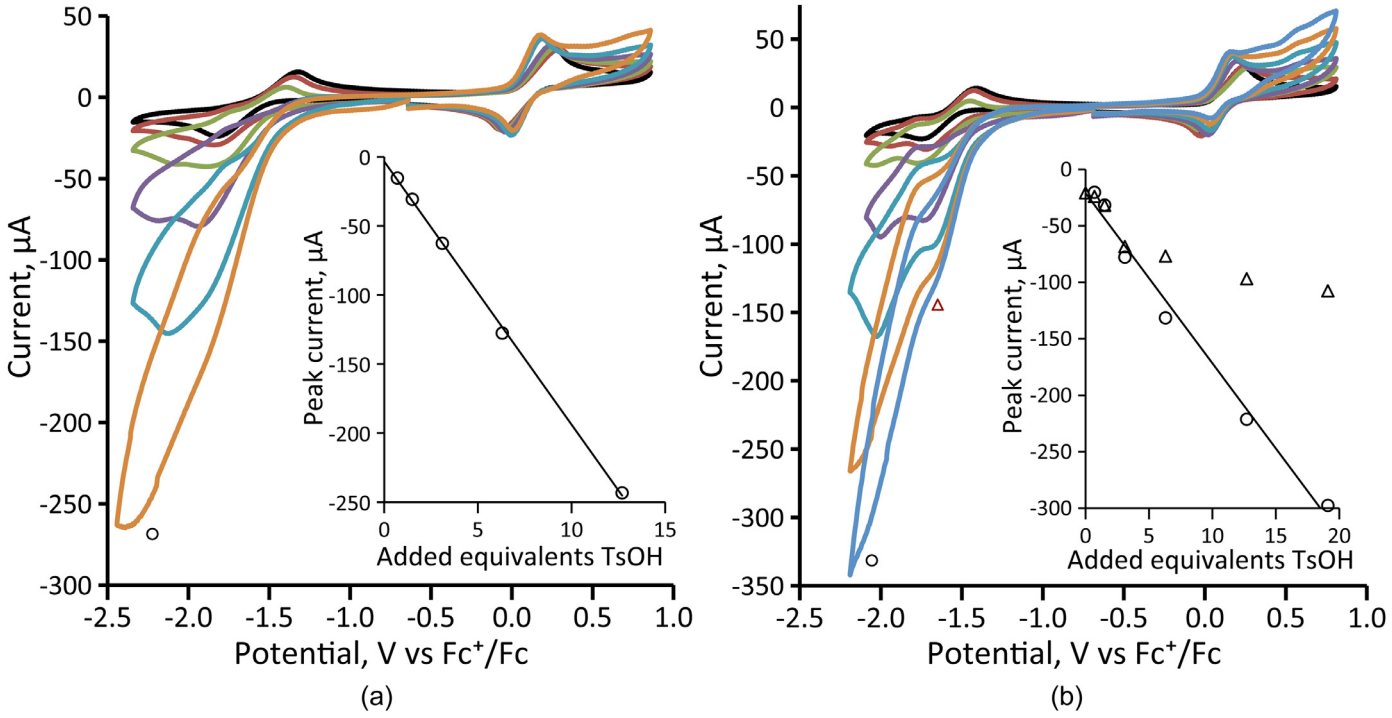

Fig. 8. Cyclic voltammograms of complexes (a) $[Fe_3(CO)_7(\mu_3\text{-PPh})_2(\kappa^2\text{-dppb})]$ (2, 2 mM) and (b) $[Fe_3(CO)_7(\mu_3\text{-PPh})_2(\kappa^2\text{-dppv})]$ (3, 2 mM) in the absence and presence of 1–19 molar equivalents of *p*-TsOH (1 mM solution in CH_2Cl_2 supporting electrolyte $[NBu_4][PF_6]$, scan rate 0.25 Vs^{-1}, glassy carbon electrode, potential *vs* Fc^+/Fc).

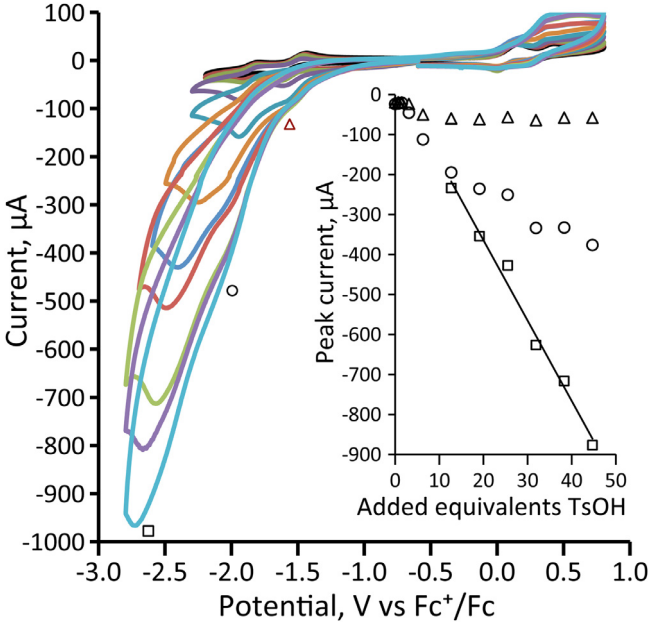

Fig. 9. CVs of complex $[Fe_3(CO)_7(\mu_3\text{-PPh})_2(\kappa^2\text{-dppe})]$ (4) (2 mM) in the absence and presence of 1-45 molar equivalents of *p*-TsOH in CH_2Cl_2, supporting electrolyte $[NBu_4][PF_6]$, scan rate 0.25 Vs^{-1}, glassy carbon electrode, potential *vs* Fc^+/Fc).

suggests that the active species is derived from reduction of a protonation product such as $(4 + mH^+ + ne)^{(n\text{-}m)-}$ where ($n \geq 3$ and $m < n$). The available data do not determine between protonation in the active species at a capping or bridging phosphinidene phosphorus or iron atom. Infrared spectra of 4 in dichloromethane solution are unperturbed by addition of acid; *i.e.*, the neutral cluster 4 is not protonated by *p*-TsOH. It is not possible to characterize the products of protonation of $4^{\bullet-}$ or 4^{*2-}, because these species are competent for H_2-evolution (leading to the first and second catalytic waves, respectively).

The nature of the one- and two-electron reduction products originating from species **A** was explored in more detail by DFT calculations. The optimized structures of the reduced species $^2\mathbf{A}^-$ and $^3\mathbf{A}^{2-}$ were analyzed for their net spin densities [67]. Fig. 10 shows the spin density plots for $^2\mathbf{A}^-$ and $^3\mathbf{A}^{2-}$. The addition of one electron to **A** yields the radical anion $^2\mathbf{A}^-$ whose structure reveals a significant expansion of the Fe–Fe(CO)(PP) bond in the starting cluster $[Fe_3(CO)_7(\mu_3\text{-PMe})_2(\kappa^2\text{-dppeMe}_4)]$. The initial Fe–Fe(CO)(PP) bond distance of 2.729 Å in **A** increases to 3.328 Å in $^2\mathbf{A}^-$, resulting in a weakening of this Fe–Fe bond. The WBI for the Fe–Fe(CO)(PP) bond decreases by 50% (WBI = 0.14) upon electron accession. The other Fe–Fe bond and the internuclear distance between the non-bonded, wingtip iron centers in $^2\mathbf{A}^-$ are not significantly affected based on WBIs of 0.31 and 0.05. These latter values closely mirror the WBIs computed for neutral **A**. This regiospecific elongation of the Fe–Fe(CO)(PP) bond in $^2\mathbf{A}^-$ helps eliminate steric congestion between the metallic centers in the Fe–Fe(CO)(PP) vector. The spin density plot of $^2\mathbf{A}^-$ confirms that the majority of spin is located on the iron atom of the Fe(CO)(PP) moiety, along with a minor contribution from the CO ligand in the Fe(CO)(PP) moiety. The uptake of a second electron furnishes the dianion that can exist as a diamagnetic singlet ($\mathbf{A}^{2-}$) or a triplet dianion ($^3\mathbf{A}^{2-}$). Both species were successfully optimized, and the triplet dianion was computed to lie 14.1 kcal/mol (ΔG) lower in energy than the corresponding singlet dianion. The large increase in the spin density at the iron atom and CO ligand of the Fe(CO)(PP) moiety in $^3\mathbf{A}^{2-}$ indicates that the addition of the second electron occurs predominantly at these sites. The iron site in the Fe(CO)(PP) moiety of the reduced species $^2\mathbf{A}^-$ and $^3\mathbf{A}^{2-}$ is electron rich and can serve as the initial site for protonation in the presence of added acid, followed by the ultimate release of H_2.

CVs for cluster 5 with increasing acid (*p*-TsOH) are presented in Figure S9. As increasing acid was added, the reduction at –1.89 V became more irreversible and grew in current reaching a

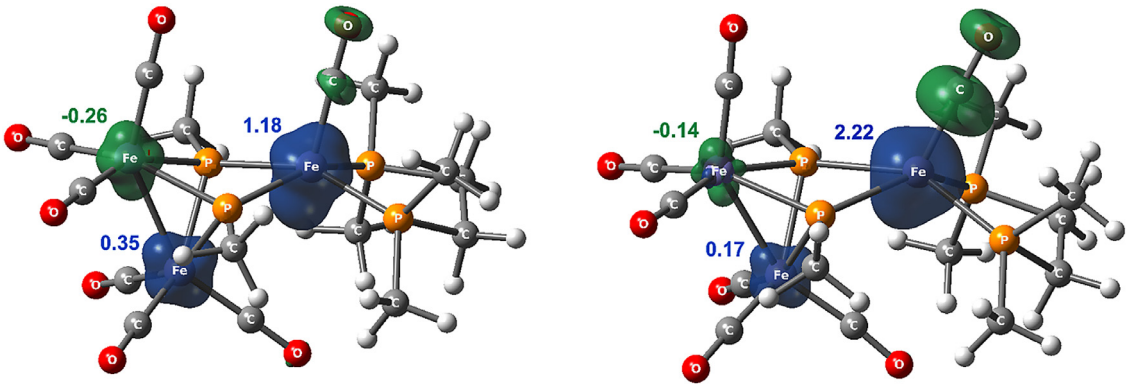

Fig. 10. Spin density plots for radical anion $^{2}\mathbf{A}^{-}$ (left) and the triplet dianion $^{3}\mathbf{A}^{2-}$ (right).

maximum $i^{cat}/i^{0} \approx 8$ at *ca* 32 equiv. of acid. Interestingly, the second and, particularly, the third oxidation couples of 5 were also perturbed by the acid, with the anodic currents increasing and the chemical reversibility decreasing. The result may indicate that the cluster decomposes upon oxidation in the presence of acid.

4. Summary and conclusions

The bicapped triiron cluster $[Fe_3(CO)_9(\mu_3\text{-PPh})_2]$ (1) and new electron rich derivatives of 1 formed by substitution with chelating diphosphines have been prepared. All clusters are capped by an *anti*-arrangement of two triply bridging μ_3-PPh phosphinidene ligands. The diphosphines coordinate in a chelating (dppb, 2; dppv, 3; dppe; 4) or a bridging (dppf, 5) mode, as established by X-ray crystallography for 3 and 5. The dppb ligand also coordinates in a chelating mode in the crystal structure of cluster 2', a derivative of 2 containing an unusual phosphinidene-oxido ligand formed by the insertion of an oxygen atom into a metal-phosphorus bond; the source of the oxygen atom and the mechanism of formation of 2' are unclear. All complexes have been examined as proton reduction catalysts in the presence of *p*-TsOH in CH_2Cl_2. Cluster 1 undergoes successive, quasi-reversible, 1-electron reductions to produce the anion radical $1^{\bullet-}$ and the triplet dianion 1^{2-} at –1.39 V and –1.66 V, respectively. Both species appear competent for catalysis of proton reduction, but the catalytic current at the primary reduction at –1.39 V is low, indicative of low turnover at this potential. The diphosphine-substituted clusters 2–5 exhibit different electrochemical and electrocatalytic behaviour. The primary reduction processes appear at more negative potential than for 1, consistent with the build-up of electron density in the Fe_3 cluster core upon diphosphine substitution. Clusters 2 and 3 show a single quasi-reversible reduction couple at *ca.* –1.7 V. In the presence of *p*-TsOH, strong catalytic waves for proton reduction are observed at the potential of this primary reduction. The stronger catalytic waves upon reduction of 2 and 3 compared to 1 may be correlated with the build-up of cluster core electron density, and thus more rapid protonation leading to hydrogen evolution. Cluster 4 shows three reductive processes; in the presence of *p*-TsOH, only a weak catalytic wave at the first reduction potential at –1.6 V was observed and a much larger catalytic current appears at –2.0 V where the reduction of a successor species produced at the first reduction occurs. A third, stronger, catalytic wave appears at higher acid concentration but at very negative voltage where direct reduction of *p*-TsOH may also occur. A close scrutiny of the electrocatalysis experiments for 2 and 3 (Fig. 8) suggests that their electrocatalytic behaviour is similar to that of 4, but less clear and pronounced. Cluster 5 shows only a single reduction process at –1.95 V, which gave only a weak catalytic current in the presence of acid. The results fit with the notion that reduction at more negative potential leads, in general, to more electron rich species that are more rapidly protonated, and thus faster proton reduction catalysis. The compromise is that more negative potential corresponds to higher energy consumption. There are interesting details in these results, such as the differences and similarities in the behaviours of clusters 2–5, which warrant further investigation.

Appendix A. Supplementary data

Supplementary data to this article, including an MPEG4 movie of the electrocatalytic response during proton reduction by $[Fe_3(CO)_9(\mu_3\text{-PPh})_2]$ (1), can be found online at https://doi.org/10.1016/j.jorganchem.2019.XXXX. CCDC entries no 1896754, 1896755 and 1896756 contain the supplementary crystallographic data for 2', 3 and 5, respectively. Copies of this information may be obtained free of charge from The Director, CCDC, 12 Union Road, Cambridge, CB2 1EZ, UK (fax: +44-1223-336033; e-mail: deposit@ccdc.cam.ac.uk or http://www.ccdc.cam.ac.uk). Atomic coordinates and energies for all DFT-optimized structures are available upon request (MGR).

Declaration of Competing Interest

The authors declare no competing interests.

Acknowledgements

We thank the European Commission for the award of an Erasmus Mundus pre-doctoral fellowship to AR and MGR thanks the Robert A. Welch Foundation (Grant B-1093) for funding. The DFT calculations were performed at UNT through CASCaM, which is an NSF-supported facility (CHE-1531468). We also wish to thank Dr. David A. Hrovat who prepared the spin density plots reported here.

Supplementary materials

Supplementary material associated with this article can be found, in the online version, at doi:10.1016/j.jorganchem.2021.121816.

References

[1] C. Tard, C.J. Pickett, Chem. Rev. 109 (2009) 2245–2274.
[2] J.A. Cracknell, K.A. Vincent, F.A. Armstrong, Chem. Rev. 108 (2008) 2439–2461.
[3] P.M. Vignais, B. Billoud, Chem. Rev. 107 (2007) 4206–4272.
[4] M. Frey, ChemBioChem 3 (2002) 153–160.
[5] J.W. Peters, Curr. Opin. Struct. Biol. 9 (1999) 670–676.
[6] Y. Nicolet, C. Cavazza, J.C. Fontecilla-Camps, J. Inorg. Biochem. 91 (2002) 1–8.
[7] J.W. Peters, W.N. Lanzilotta, B.J. Lemon, L.C. Seefeldt, Science 282 (1998) 1853–1858.

[8] (a) I.P. Georgakaki, L.M. Thomson, E.J. Lyon, M.B. Hall, M.Y. Darensbourg, Coord. Chem. Rev. 238-239 (2003) 255–266; (b) D.J. Evans, C.J. Pickett, Chem. Soc. Rev. 32 (2003) 268–275; (c) T.B. Rauchfuss, Inorg. Chem. 43 (2004) 14–26; (d) L. Sun, B. Åkermark, S. Ott, Coord. Chem. Rev. 249 (2005) 1653–1663; (e) X. Liu, S.K. Ibrahim, C. Tard, C.J. Pickett, Coord. Chem. Rev 249 (2005) 1641–1652; (f) Y. Nicolet, C. Piras, P. Legrand, C.E. Hatchikian, J.C. Fontecilla–Camps, Structure 7 (1999) 13–23.

[9] (a) A. Rahaman, G.C. Lisensky, D.A. Tocher, M.G. Richmond, G. Hogarth, E. Nordlander, J. Organomet. Chem. 867 (2018) 381–390; (b) S. Ghosh, A. Rahaman, K.B. Holt, E. Nordlander, M.G. Richmond, S.E. Kabir, G. Hogarth, Polyhedron 116 (2016) 127–135.

[10] (a) M. Bruschi, C. Greco, M. Kaukonen, P. Fantucci, U. Ryde, L.De. Gioia, Angew. Chem. 121 (2009) 3555–3558; (b) C. Greco, P. Fantucci, L.De. Gioia, R.S. Bertoa, M. Bruschi, J. Talarmin, P. Schollhammer, Dalton Trans. 39 (2010) 7320–7329; (c) C. Greco, G. Zampella, L. Bertini, M. Bruschi, P. Fantucci, L. De Gioia, Inorg. Chem. 46 (2007) 108–116.

[11] C. Tard, X. Liu, D.L. Hughes, C.J. Pickett, Chem. Commun. (2005) 133–135.

[12] (a) A. Rahaman, S. Ghosh, D.G. Unwin, K.B.Holt S.B.-Modi, S.E. Kabir, E. Nordlander, M.G. Richmond, G. Hogarth, Organometallics 33 (2014) 1356–1366; (b) S. Ghosh, G. Hogarth, K.B. Holt, S.E. Kabir, A. Rahaman, D.G. Unwin, Chem. Commun. 47 (2011) 11222–11224; (c) A. Rahaman, S. Ghosh, S.B. Modi, A.F. Abdel-Magied, S.E. Kabir, M. Haukka, M.G. Richmond, G.C. Lisensky, E. Nordlander, G. Hogarth, J. Organomet. Chem. 880 (2019) 213–222.

[13] (a) J.-F. Capon, F. Gloaguen, F.Y Pétillon, P. Schollhammer, J. Talarmin, Coord. Chem. Rev. 253 (2009) 1476–1494; (b) G.A.N. Felton, C.A. Mebi, B.J. Petro, A.K. Vannucci, D.H. Evans, R.S. Glass, D.L. Lichtenberger, J. Organomet. Chem. 694 (2009) 2681–2699.

[14] (a) M.K. Harb, T. Niksch, J. Windhager, H. Görls, R. Holze, L.T. Lockett, N. Okumura, D.H. Evans, R.S. Glass, D.L. Lichtenberger, M. El-Khateeb, W. Weigand, Organometallics 28 (2009) 1039–1048; (b) M.K. Harb, U.-P. Apfel, J. Kübel, H. Görls, G.A.N. Felton, T. Sakamoto, D.H. Evans, R.S. Glass, D.L. Lichtenberger, M. El-Khateeb, W. Weigand, Organometallics 28 (2009) 6666–6675.

[15] L.-C. Song, B. Gai, Z.-H. Feng, Z.-Q. Du, Z.-J. Xie, X.-J. Sun, H.-B. Song, Organometallics 32 (2013) 3673–3684.

[16] (a) C.M. Thomas, O. Rüdiger, T. Liu, C.E. Carson, M.B. Hall, M.Y. Darensbourg, Organometallics 26 (2007) 3976–3984; (b) L.-C. Song, Q.-L. Li, Z.-H. Feng, X.-J. Sun, Z.-J. Xie, H.-B. Song, Dalton Trans. 42 (2013) 1612–1626.

[17] M.K. Harb, H. Görls, T. Sakamoto, G.A.N. Felton, D.H. Evans, R.S. Glass, D.L. Lichtenberger, M. El- Khateeb, W. Weigand, Eur. J. Inorg. Chem. 25 (2010) 3976–3985.

[18] (a) D. Seyferth, T.G. Wood, J.P. Fackler Jr, A.M. Mazany, Organometallics 3 (1984) 1121–1123; (b) D. Seyferth, T.G. Wood, R.S. Henderson, J. Organomet. Chem. 336 (1987) 163–182.

[19] (a) D. Seyferth, T.G. Wood, Organometallics 6 (1987) 2563–2567; (b) D. Seyferth, T.G. Wood, Organometallics 7 (1988) 714–718; (c) R.D. Adam, S. Wang, Inorg. Chem. 24 (1985) 4449–4450; (d) R.B. King, F.-J. Wu, E.M. Holt, Inorg. Chem. 25 (1986) 1733–1734; (e) R.B. King, F.-J. Wu, E.M. Holt, J. Am. Chem. Soc. 109 (1987) 7764–7775; (f) J.S. McKennis, E.P. Kyba, Organometallics 2 (1983) 1249–1251; (g) E.P. Kyba, R.E. Davis, C.N. Clubb, S.-T. Liu, H.O.A. Palacios, J.S. McKennis, Organometallics 5 (1986) 869–877; (h) E.P. Kyba, M.C. Kerby, S.P. Rines, Organometallics 5 (1986) 1189–1194; (i) T.C. Flood, F.J. Disanti, K.D. Campbell, Inorg. Chem 17 (1978) 1643–1646; (j) A.L. Rheingold, Acta Crystallogr. C41 (1985) 1043–1045; (k) P.M. Treichel, W.M. Douglas, W.K. Dean, Inorg. Chem. 11 (1972) 1615–1618.

[20] (a) D. Seyferth, R.S. Henderson, L.-C. Song, Organometallics 1 (1982) 125–133; (b) D. Seyferth, G.B. Womack, R.S. Henderson, M. Cowie, B.W. Hames, Organometallics 5 (1986) 1568–1575.

[21] (a) J.D. Lawrence, H. Li, T.B. Rauchfuss, Chem. Commun. (2001) 1482–1483; (b) L. Hongxiang, T.B. Rauchfuss, J. Am. Chem. Soc. 124 (2002) 726–727; (c) J.D. Lawrence, L. Hongxiang, T.B. Rauchfuss, M. Bénard, M.-M. Rohmer, Angew. Chem. Int. Ed. 40 (2001) 1768–1771; (d) S. Ott, M. Kritikos, B. Åkermark, L. Sun, Angew. Chem., Int. Ed. 42 (2003) 3285–3288; (e) S. Ott, M. Borgström, M. Kritikos, R. Lomoth, J. Bergquist, B. Åkermark, L. Hammarström, L. Sun, Inorg. Chem. 43 (2004) 4683–4692.

[22] (a) P.M. Treichel, W.K. Dean, W.M. Douglas, Inorg. Chem. 11 (1972) 1609–1615; (b) R. Bartsch, S. Hietkamp, S. Morton, O. Stelzer, J. Organomet. Chem. 222 (1981) 263–273; (c) J.P. Collman, R.K. Rothrock, R.G. Finke, E.J. Moore, F. Rose–Munch, Inorg. Chem. 21 (1982) 146–156; (d) P.E. Garrou, Chem. Rev. 81 (1981) 229–266.

[23] (a) W. Clegg, Inorg. Chem. 15 (1976) 1609–1613; (b) M.R. Adams, J. Gallucci, A. Wojcicki, G.J. Long, Inorg. Chem. 31 (1992) 2–4; (c) R.E. Ginsburg, R.K. Rothrock, R.G Finke, J.P. Collman, L.F. Dahl, J. Am. Chem. Soc. 101 (1979) 6550–6562.

[24] (a) R.E. Dessy, R. Kornmann, C. Smith, R. Haytor, J. Am. Chem. Soc. 90 (1968) 2001–2004; (b) Y.F. Yu, J. Gallucci, A. Wojcicki, J. Am. Chem. Soc 105 (1983) 4826–4828; (c) M.-H. Baik, T. Ziegler, C.K. Schauer, J. Am. Chem. Soc. 122 (2000) 9143–9154; (d) S.G. Shyu, A. Wojcicki, Organometallics 4 (1985) 1457–1459; (e) A. Wojcicki, Inorg. Chim. Acta 100 (1985) 125–133.

[25] R. Zaffaroni, T.B. Rauchfuss, A. Fuller, L. De Gioia, G. Zampella, Organometallics 32 (2013) 232–238.

[26] J.G.M. Van der Linden, J. Heck, B. Walther, H.-C. Böttcher, Inorg. Chim. Acta 217 (1994) 29–32.

[27] P. Das, J.-F. Capon, F. Gloaguen, F.Y. Pétillon, P. Schollhammer, J. Talarmin, K.W. Muir, Inorg. Chem. 43 (2004) 8203–8205.

[28] M.H. Cheah, S.J. Borg, S.P. Best, Inorg. Chem. 46 (2007) 1741–1750.

[29] M.H. Cheah, S.J. Borg, M.I. Bondin, S.P. Best, Inorg. Chem. 43 (2004) 5635–5644.

[30] R.E. Ginsburg, R.K. Rothrock, R.G. Finke, J.P. Collman, L.F. Dahl, J. Am. Chem. Soc. 101 (22) (1979) 6550–6562.

[31] Y.-C. Shi, W. Yang, Y. Shi, D.-C. Cheng, J. Coord. Chem. 67 (2014) 2330–2343.

[32] C.G. Suriñach, M. Bhadbhade, S.B. Colbran, Organometallics 31 (2012) 3480–3491.

[33] A. Rahaman, C.G. Suriñach, A. Ficks, G.E. Ball, M. Bhadbhade, M. Haukka, L. Higham, E. Nordlander, S.B. Colbran, Dalton Trans 46 (2017) 3207–3222.

[34] V.D. Patel, A.A. Cherkas, D. Nucciarone, N.J. Taylor, A.J. Carty, Organometallics 4 (1985) 1792–1800.

[35] M. Shieh, C.-H. Ho, W.-S. Sheu, B.-G. Chen, Y.-Y. Chu, C.-Y. Miu, H.-L. Liu, C.-C. Shen, J. Am. Chem. Soc. 130 (2008) 14114–14116.

[36] C.C. Borg-Breen, M.T. Bautista, C.K. Schauer, P.S. White, J. Am. Chem. Soc 122 (2000) 3952–3962.

[37] G.D. Williams, G.L. Geoffroy, R.R. Whittle, A.L. Rheingold, J. Am. Chem. Soc. 107 (1985) 729–731.

[38] M.T. Bautista, P.S. White, C.K. Schauer, J. Am. Chem. Soc. 113 (23) (1991) 8963–8965.

[39] (a) H.H. Ohst, J.K. Kochi, J. Chem. Soc., Chem. Commun. (1986) 121–123; (b) H.H. Ohst, J.K. Kochi, J. Am. Chem. Soc. 108 (1986) 2908–2916.

[40] M. Shieh, C.-Y. Miu, K.-C. Huang, C.-F. Lee, B.-G. Chen, Inorg. Chem. 50 (16) (2011) 7735–7748.

[41] J.L. Perkinson, M.H. Baik, G.E. Trullinger, C.K. Schauer, P.S. White, Inorg. Chim. Acta. 294 (1999) 140–152.

[42] N.A. Pushkarevsky, D.A. Bashirov, T.G. Terent'eva, A.V. Virovets, E.V. Peresypkina, H. Krautscheid, S.N. Konchenko, Russ. J. Coord. Chem. 32 (2006) 416–426.

[43] H.H. Ohst, J.K. Kochi, Inorg. Chem. 25 (1986) 2066–2074.

[44] W. Gao, J. Sun, M. Li, T. Åkermark, K. Romare, L. Sun, B. Åkermark, Eur. J. Inorg. Chem (2011) 1100–1105.

[45] R.M. De Silva, M.J. Mays, G.A. Solan, J. Organomet. Chem. 664 (2002) 27–36.

[46] S.L. Cook, J. Evans, L.R. Gray, M. Webster, J. Organomet. Chem. 236 (1982) 367–374.

[47] Bruker AXSAPEX2-Software Suite for Crystallographic Programs, Bruker AXS, Inc. Madison, WI, USA, 2009.

[48] AgilentCrysAlisPro, Agilent Technologies inc, Yarnton, Oxfordshire, England, 2014.

[49] G.M. Sheldrick, Acta Cryst A64 (2008) 112–122.

[50] L. Palatinus, G. Chapuis, J. Appl. Cryst. 40 (2007) 786–790.

[51] G.M. Sheldrick, SADABS - Bruker Nonius scaling and absorption correction, Bruker AXS, Inc., Madison, Wisconsin, USA, 2012.

[52] Y. Zhao, D.G. Truhlar, Theor. Chem. Acc. 120 (2008) 215–241.

[53] M.J. Frisch, et al., Gaussian 09, Revision E.01, Gaussian, Inc., Wallingford, CT, USA, 2009.

[54] D. Andrae, U. Haeussermann, M. Dolg, H. Stoll, H. Preuss, Theor. Chim. Acta 77 (1990) 123–141.

[55] (a) G.A. Petersson, A. Bennett, T.G. Tensfeldt, M.A. Al-Laham, W.A. Shirley, J. Mantzaris, J. Chem. Phys. 89 (1988) 2193–2218; (b) G.A. Petersson, M.A. Al-Laham, J. Chem. Phys. 94 (1991) 6081–6090.

[56] S. Grimme, S. Ehrlich, L. Goerigk, J. Comp. Chem. 32 (2011) 1456–1465.

[57] A.E. Reed, L.A. Curtiss, F. Weinhold, Chem. Rev. 88 (1988) 899–926.

[58] K.B. Wiberg, Tetrahedron 24 (1968) 1083–1096.

[59] (a) M.B. Hall, R.F. Fenske, JIMP2, version 0.091, a free program for the visualization and manipulation of molecules:, Inorg. Chem. 11 (1972) 768–775; (b)J. Manson, C.E. Webster, M.B. Hall, Texas A&M University, College Station, TX, 2006, http://www.chem.tamu.edu/jimp2/index.html.

[60] N. Begum, U.K. Das, M. Hassan, G. Hogarth, S.E. Kabir, E. Nordlander, D.A. Tocher, Organometallics 26 (25) (2007) 6462–6472.

[61] V. Moberg, P. Homanen, S. Selva, R. Persson, M. Haukka, T.A. Pakkanen, M. Monari, E. Nordlander, Dalton Trans (2006) 279–288.

[62] C.H. Wei, L.F. Dahl, Inorg. Chem. 4 (1965) 493–499.

[63] J.P. Foster, F. Weinhold, J. Am. Chem. Soc. 102 (1980) 7211–7218.

[64] (a) K.B. Wiberg, Tetrahedron 24 (1968) 1083–1096; (b) I. Mayer, J. Comput. Chem. 28 (2007) 204–221.

[65] A. Rahaman, G.C. Lisensky, J. Browder-Long, D.A Hrovat, M.G. Richmond, E. Nordlander, G. Hogarth, Dalton Trans 49 (21) (2020) 7133–7143.

[66] (a) S. Ghosh, G. Hogarth, N. Hollingsworth, K.B. Holt, S.E. Kabir, B.E. Sanchez, Chem. Commun. 50 (2014) 945–947; (b) A.C. Ohs, A.L. Rheingold, M.J. Shaw, C. Nataro, Organometallics 23 (2004) 4655–4660; (c) D.L. DuBois, C.W. Eigenbrot, J.A. Miedaner, J.C. Smart, R.C. Haltiwanger, Organometallics 5 (1986) 1405–1411; (d) B.D. Swartz, C. Nataro, Organometallics 24 (2005) 2447–2451; (e) C. Nataro, A.N. Campbell, M.A. Ferguson, C.D. Incarvito, A.L. Rheingold, J. Organomet. Chem. 673 (2003) 47–55; (f) G. Pilloni, B. Longato, B. Corain, J. Organomet. Chem 420 (1991) 57–65; (g) B. Corain, B. Longato, G. Favero, D. Ajò, G. Pilloni, U. Russo, F.R. Kreissl, Inorg. Chim. Acta. 157 (1989) 259–266.

[67] In the odd electron species **2A–** and **3A2–** the integer superscripts 2 and 3 refer to the doublet and triplet spin states, respectively, while the remaining superscripts define the overall charge on each species.